EDGE ARTICLE

Check for updates

Planar hexacoordinate gallium†

Meng-hui Wang,[a] Chen Chen,[a] Sudip Pan [ID] *[bc] and Zhong-hua Cui [ID] *[ad]

We report the first planar hexacoordinate gallium (phGa) center in the global minimum of the $GaBe_6Au_6^+$ cluster which has a star-like D_{6h} geometry with $^1A_{1g}$ electronic state, possessing a central gallium atom encompassed by a Be_6 hexagon and each Be–Be edge is further capped by an Au atom. The electronic delocalization resulting in double aromaticity (both σ and π) provides electronic stability in the planar form of the $GaBe_6Au_6^+$ cluster. The high kinetic stability of the title cluster is also understood by Born–Oppenheimer molecular dynamics simulations. The energy decomposition analysis in combination with the 'natural orbitals for chemical valence' theory reveals that the bonding in the $GaBe_6Au_6^+$ cluster is best expressed as the doublet Ga atom with $4s^24p_\perp^1$ electronic configuration forming an electron-sharing π bond with the doublet $Be_6Au_6^+$ moiety followed by Ga(s)$\rightarrow$[$Be_6Au_6^+$] σ-backdonation and two sets of Ga(p$_\parallel$)$\leftarrow$[$Be_6Au_6^+$] σ-donations.

Introduction

The creative mind is always fascinated in breaking the usual established rules, supported by the traditional knowledge, to set a new limit to break. That is the way science is progressing. In chemistry, the realization of planar tetracoordination for carbon, in contrast to the usual tetrahedral arrangement, was one of such events that arose much curiosity in the scientific community in the late twentieth century when Hoffmann *et al.*,[1] in their hallmark paper published in 1970, put forward the effective electronic stabilization strategy for planar tetra-coordinate carbon (ptC). Over the past half century, persistent research and great efforts were made by several groups in this area, which led to the detection or synthesis and/or theoretical prediction of a variety of planar hypercoordinate carbon and other elements.[2–27] Amongst them, there are numerous successful examples (global structure) in the literature for the planar tetracoordinate (pt) species[4–6,28–45] and even some of them (CAl_4^-, CAl_4^{2-}, CAl_3Si^-, CAl_3Ge^- and CAl_4H^-)[46–50] were detected in the gas-phase. Research is not only restricted to carbon, but anionic ptAl[15] and neutral ptSi[16–18] were also synthesized which could show astonishing reactivities as well. If achievement of planar tetracoordinate centers is elegant, the

designing of planar hypercoordinate species beyond tetra-coordination is no less than an artist's imagination in an excellent mood. Focusing on groups 13 and 14 elements, such hypercoordination violates both the usual coordination number and geometry (*tricoordinates* and *trigonal geometry* for the former and *tetracoordinates* and *tetrahedral geometry* for the latter case).

The achievement of planar hypercoordinate species essentially benefits from the electronic or steric stabilization strategy, or a combination of both.[1] In other words, the electronic and structural match between the planar center and ligand ring is a key factor for designing planar hypercoordinate species, especially the prerequisites become much more crucial with the increasing coordination number since they clearly violate both conventional bonding constraints simultaneously. Indeed, in contrast to numerous planar tetracoordinate species, only a few higher coordinated species have been reported so far, and mostly for planar pentacoordinate (pp) motifs.[2,3,23,24,51–60] CAl_5^+ is the first masterpiece which possesses ppC in its global minimum.[19] Readers can further refer to a recent review to know the present status of ppC systems.[2]

The realization of a planar hexacoordinate (ph) bonding motif, that is both thermodynamically and kinetically stable, is extremely rare.[23,24] The research in that direction was triggered by the theoretical report of CB_6^{2-} containing a phC[25] which later turned out to be a high-lying isomer.[60] The first true global minimum phC was found in the D_{3h} symmetric $CO_3Li_3^+$ cluster,[24] although there is some doubt whether the C–Li linkage can be called a true coordination because of electro-static repulsion originating from the positively charged phC and Li centers. Recently Tiznado and co-workers reported a series of global minimum for $CE_3M_3^+$ (E = S, Se, Te; M = Li–Cs) having phC where the phC center carries a negative charge, and therefore, it induces electrostatic attraction between phC and

[a] Institute of Atomic and Molecular Physics, Key Laboratory of Physics and Technology for Advanced Batteries (Ministry of Education), Jilin University, Changchun, China. E-mail: zcui@jlu.edu.cn

[b] Institute of Advanced Synthesis, School of Chemistry and Molecular Engineering, Jiangsu National Synergetic Innovation Center for Advanced Materials, Nanjing Tech University, Nanjing, China

[c] Fachbereich Chemie, Philipps-Universität Marburg, Hans-Meerwein-Strasse 4, 35032 Marburg, Germany. E-mail: pans@chemie.uni-marburg.de

[d] Beijing National Laboratory for Molecular Sciences, China

† Electronic supplementary information (ESI) available. See DOI: 10.1039/d1sc05089c

alkali atoms.[23] In these clusters, phC is multiply bonded to three chalcogens and ionically connected to the three alkali metals. Planar hypercoordinate boron in all-boron clusters is common because of the remarkable ability of boron to form planar structures even for much larger clusters and to form multi-centered delocalized bonds owing to its inherent electron defi-cient nature.[61] The planar hexacoordinate boron that is relevant to the present study is the most stable isomer of $BBe_6H_6^+$ with a phB center and having dual ($\sigma + \pi$) aromaticity.[26,27] A cluster containing a phAl in the global minimum form of the Al_4C_6 cluster was also reported.[62] Apart from these, planar hex-acoordination in an isolated cluster was not found. Note that the planar hexacoordinate motifs can be embedded in a two-dimensional (2D) nanosheet,[63–65] which can provide both elec-tronic stabilization and electronic-stabilization-induced steric force supports.[65] But that is a different story as compared to the isolated clusters, which basically only rely on the electronic stabilization strategy, making their design extremely challengeable.

Herein, we report a thermodynamically and kinetically stable phGa cluster. To locate the planar hexacoordinate motifs, the appropriate peripheral ligand is a key factor, for example, the good π-acceptor/σ-donor capability (electronic factor) and strong ligand–ligand bond for the self-stability of the peripheral ligand ring (mechanical factor) could be the best target. In the light of the great superiority (real minimum) and clear limit (high-lying structure) of a boron monocyclic ring in the forma-tion of planar hypercoordinate species, we systematically tested the possibility of using a beryllium ring (Be_n), decorated by bridging s-block atoms (being isoelectronic to the boron monocyclic ring), in the planar hexacoordinate bonding. The global minimum of the $GaBe_6Au_6^+$ cluster has a star-like D_{6h} geometry with a $^1A_{1g}$ electronic state, possessing a central gallium atom encompassed by a Be_6 hexagon and each Be–Be edge is further capped by an Au atom. The other group 13 elements do not lead to a planar hexacoordinate moiety as the most stable isomer.

Computational details

The structure search was performed using the CALYPSO (Crystal Structure Analysis by Particle Swarm Optimization) code, where the particle swarm optimization algorithm is implemented.[66,67] PBE0/def2-SVP[68,69] was used to optimize the initial structure of $EBe_6Au_6^+$ (E = Al, Ga, In, Tl) with singlet and triplet spin states, and for the low-lying (within 40 kcal mol^{-1} relative energy window with respect to the global minimum) isomers we employed a bigger def2-TZVP basis set for better geometrical and frequency prediction. The single-point calcu-lations for the low-lying energy isomers were performed at the CCSD(T)/def2-TZVP//PBE0/def2-TZVP level.[69,70] Total energies were corrected using the zero-point energies (ZPEs) obtained at the PBE0/def2-TZVP level. Note that since we are comparing relative energies between two isomers, the relative error intro-duced in the results for adding ZPEs at the DFT level to the CCSD(T) energies will also be minimized. All these calculations were carried out with the Gaussian 09 program package.[71] The

natural bond orbital analysis for phGa was performed by using the NBO 7.0 program.[72–74] The electron localization function (ELF) and the quantum theory of atoms in molecules (QTAIM)[75,76] analyses were done using the Multiwfn program.[77]

The Born–Oppenheimer molecular dynamics (BO-MD) simulation[78] was carried out at temperatures of 300 and 400 K at the PBE0/def2-SVP level. Each simulation ran for 10 ps with a step size of 0.5 fs from the equilibrium global minimum structure with random velocities assigned to the atoms according to a Maxwell–Boltzmann distribution for both temperatures, and then normalized so that the net angular momentum for the whole system is zero. BO-MD simulations were performed using Gaussian 09 software.[71]

The energy decomposition analysis (EDA)[79] in combination with the natural orbitals for chemical valence (NOCV)[80] method was performed at the PBE0/TZ2P-ZORA//PBE0/def2-TZVP level using the ADF (2018.105) program package.[81,82] In the EDA method, the interaction energy (ΔE_{int}) between two prepared fragments is divided into three energy terms, viz., the electro-static interaction energy (ΔE_{elstat}), which represents the quasi-classical electrostatic interaction between the unperturbed charge distributions of the prepared atoms, the Pauli repulsion (ΔE_{Pauli}), which is the energy change associated with the transformation from the superposition of the unperturbed electron densities of the isolated fragments into the wave-function that properly obeys the Pauli principle through explicit antisymmetrization and renormalization of the product wave-function, and the orbital interaction energy (ΔE_{orb}), which originates from the mixing of orbitals, charge transfer and polarization between the isolated fragments. Therefore, the interaction energy (ΔE_{int}) between two fragments can be defined as:

$$\Delta E_{int} = \Delta E_{elstat} + \Delta E_{Pauli} + \Delta E_{orb} \tag{1}$$

The orbital term may be further divided into contributions from each irreducible representation of the point group of the interacting system as follows:

$$\Delta E_{orb} = \sum_r \Delta E_r \tag{2}$$

The EDA–NOCV combination allows the partition of ΔE_{orb} into pairwise contributions of the orbital interactions, which gives important information about bonding. The charge deformation $\Delta \rho_k(r)$ which originates from the mixing of the orbital pairs $\Psi_k(r)$ and $\Psi_{-k}(r)$ of the interacting fragments gives the size and the shape of the charge flow because of the orbital interactions (eqn (3)), and the corresponding ΔE_{orb} reflects the amount of orbital interaction energy coming from such inter-action (eqn (4)).

$$\Delta \rho_{orb}(r) = \sum_k \Delta \rho_k(r) = \sum_k^{N/2} V_k \left[-\psi_{-k}^2(r) + \psi_k^2(r) \right] \tag{3}$$

$$\Delta E_{orb} = \sum_k \Delta E_k^{orb} = \sum_{k=1}^{N/2} v_k \left[-F_{-k}^{TS} + F_k^{TS} \right] \tag{4}$$

More information about the method and its applicability can be found in a recent review.[83]

Structures and stability

Firstly, we have checked the optimized geometries and nature of the stationary points for $EBe_6Au_6^+$ (E = Al, Ga, In, Tl) clusters having a phE center enclosed by a Be_6 ring with the latter being further decorated by bridging Au atoms. The resulting arrangement has a D_{6h} symmetry and $^1A_{1g}$ electronic state. It turns out that the $(BeAu)_6$ ring could indeed be a suitable peripheral ring to stabilize a phE, where the phE isomer of $EBe_6Au_6^+$ turns out to be a real minimum for E = Ga and Tl, but a transition state with one imaginary frequency of $90.2i$ and $22.0i$ cm^{-1} for E = Al and In, respectively. The mode of the imaginary frequency corresponds to the out-of-plane movement of E which leads to a quasi-planar C_{6v} symmetric structure where E is located 0.90 Å for Al and 0.98 Å for In above the Be_6 basal plane. Similar results are also obtained taking different levels, B3LYP/def2-TZVP and TPSS/def2-TZVP (see Fig. S1 in the ESI†) which confirms that this observation is not an artefact of a particular level. Note that $Be_6Au_6^q$ ($q = -1$, 0, 1) clusters without any group 13 dopant have a three-dimensional unsymmetric geometry as the most stable isomer, whereas the planar isomer having a Be_6 ring capped with Au at the bridging positions is a higher order saddle point (see Fig. S2†). Therefore, it indicates that the bonding between E and Be_6Au_6 unit is crucial to facilitate the planarization of the latter cluster.

Next, a detailed potential energy surface (PES) search for the $EBe_6Au_6^+$ (E = Al, Ga, In, Tl) clusters is performed and some low-lying isomers are provided in Fig. S3–S6.† Except for E = Ga, for others the most stable isomer is a three-dimensional cluster having a Be_5 ring with Be at the center of the ring and E located at one side of the ring. Au atoms are at the bridging position of Be–Be bonds. It is interesting to note that although for E = Tl, phTl is a minimum, it lies significantly high (by 27.0 kcal mol^{-1}) above the global minimum (see Fig. S7†). Only for $GaBe_6Au_6^+$, the D_{6h} symmetric phGa isomer turns out as the most stable isomer (see Fig. 1). It is also important to check the reliability of the single-reference based method. The T_1 diagnostic values from the converged CCSD wavefunction are reasonably small to confirm the reliability of the results (see Fig. S4†). The second and third lowest-energy ones (isomer **b** and **c**) lie 2.4 and 9.4 kcal mol^{-1} higher in energy than phGa, respectively, at the CCSD(T)/def2-TZVP//PBE0/def2-TZVP level with zero-point

energy correction of the PBE0/def2-TZVP level. The nearest triplet structure (isomer **e**) has a very high relative energy (19.1 kcal mol^{-1}) as compared to the global phGa. Therefore, the present results indicate that only for E = Ga, the interaction between Ga and Be_6Au_6 unit is strong enough to afford the large energy needed to reorient the shape of the Be_6Au_6 unit. This needs two factors to satisfy. First, the size of E atoms should be suitable to place at the center of the ring without causing significant steric repulsion, and second, E forms a sufficiently strong bond with the ring to make it energetically the most stable isomer. Note that both Al and Ga have almost similar covalent radius, but still the phAl isomer, which is a transition state, is 11.8 kcal mol^{-1} higher in energy than the three-dimensional global minimum, while the energy minimum of the C_{6v} isomer is 6.7 kcal mol^{-1} higher in energy than the most stable form (see Fig. S7†). Therefore, the bonding between Al and the outer ring must be weaker in phAl than that in phGa which can be better understood from the EDA–NOCV results (*vide infra*). It is also interesting to notice that the global minimum structure of $EBe_6Au_6^+$ for E = Al, In, Tl may be considered as the interaction of E with the most stable structure of Be_6Au_6. Only a slight alteration in structural integration occurs, E replaces Au in the axial position of Be_6Au_6 and Au is shifted to the bridging position of the Be–Be bond. In other words, only Ga has the capability to induce the drastic change in the Be_6Au_6 structure.

Another somewhat surprising observation is that although In and Tl have similar covalent radius, the D_{6h} isomer for the former case is not even a minimum, while for the latter one phTl is a true minimum, albeit significantly higher energy isomer than the global minimum. We rechecked the results with three different levels of theory and obtained similar results. The heaviest element sometimes shows anomalous behavior because of the relativistic effect. For the present cases, we attempted to shed light on the reason through the EDA–NOCV results of D_{6h} and C_{6v} isomers (*vide infra*).

To evaluate the kinetic stability of phGa, the BO-MD[78] simulations were carried out at the PBE0/def2-SVP level at 300 and 400 K. Throughout the simulation time scale, the structural integrity and planarity is well maintained, and no isomerization or other structural alterations occur as shown by the small RMSD (root mean square deviation) values in Fig. 2a (see the movies in the ESI†). The non-planar fluctuation in the BO-MD simulations correlates with the lowest vibrational mode
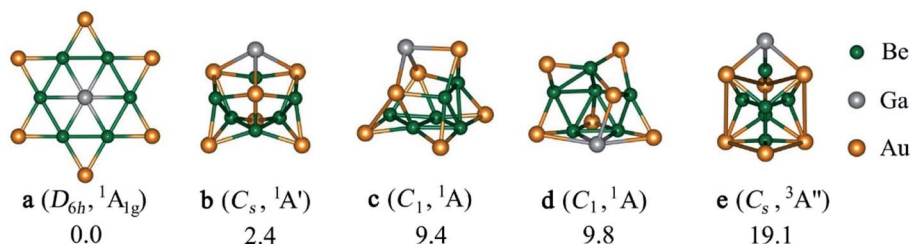

a (D_{6h}, $^1A_{1g}$) **b** (C_s, $^1A'$) **c** (C_1, ^1A) **d** (C_1, ^1A) **e** (C_s, $^3A''$)
0.0   2.4   9.4   9.8   19.1

● Be   ● Ga   ● Au

Fig. 1 The relative energies in kcal mol^{-1} of the low-lying energy isomers (a–e) of $GaBe_6Au_6^+$ computed at the CCSD(T)/def2-TZVP//PBE0/def2-TZVP with zero-point energy correction of the PBE0/def2-TZVP level.
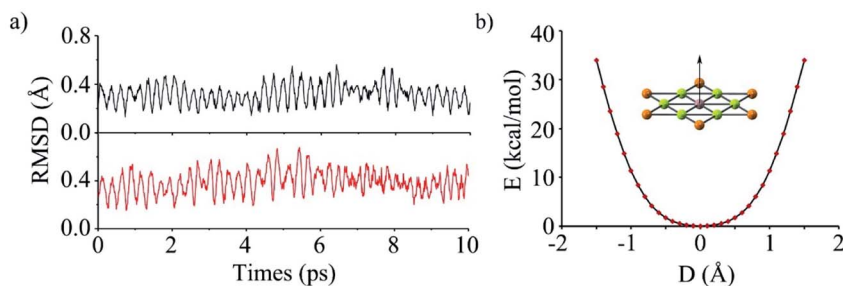
Fig. 2 (a) The RMSD *versus* time of phGa in the BOMD simulations at 300 K (black) and 400 K (red) computed at the PBE0/def2-SVP level. (b) Computed rigid energy curves of describing the out-of-plane displacement of the central Ga atom at the PBE0/def2-TZVP level.

(8.0 cm^{-1}), which is out-of-plane vibration of the phGa center. We plotted the calculated potential energy curve (PES) as a function of out-of-plane displacement of the central Ga atom as shown in Fig. 2b. It shows that the smooth PES occurs within 0.3 Å but after that it sharply goes up, indicating a perfectly planar structure of phGa to be energetically more favorable than the non-planar one. Overall, the present results reveal that phGa possesses considerable thermodynamic and kinetic stability to be suitable for experiment detection.

Bonding

Structural and electronic properties can help us to understand the reason behind the thermodynamic and kinetic stability of phGa species. Molecules with a D_{6h} symmetric planar hexacoordinate center require bond distances between two ligand centers in the hexagonal ring being equal to bond distances between the central atom and ligands, and, thus, this intriguing shape makes the design of such species not trivial. phGa $GaBe_6Au_6^+$ possesses a Ga–Be bond distance of 2.229 Å with a WBI of 0.35, suggesting the typical single bonding characteristic according to the self-consistent covalent radii of Pyykkö (2.26 Å).[84] The Be–Be and Be–Au peripheral ligand–ligand contacts have a similar bond distance in the range of 2.20–2.23 Å, yet the pronounced WBI for Be–Au (0.42) but ignorable Be–Be (0.09) suggests that strong bonding interaction between Be and bridging Au exists in the peripheral ligand ring.

For the systems containing Be atoms, the natural charges should be discussed with caution since NBO algorithm only considers the 2s orbital of Be as valence space whereas it treats 2p orbitals as Rydberg orbitals, and then it gives different weightages to the valence and Rydberg spaces, putting more priority to the former ones. However, in the present case since the cluster possesses a delocalized π orbital involving the p_z orbitals of Be (considering z axis perpendicular to the molecular plane), the natural atomic charges will not be reliable. Fig. 3 displays the partial atomic natural charges and Hirshfeld charges. Clearly, the values differ significantly. The charges computed using some other different methods are also given in Table S1.† The extent to which the values vary depending on the method is remarkable. But no other methods give such a high negative charge on Ga as NBO.

EDA–NOCV calculations were performed to understand the nature of bonding between phGa and the outer hexagonal ring. Particularly, this method gives quantitative information about the strength of each bonding component. It also allows us to assign the correct oxidation state of the phGa center. However, the choice of charge and electronic states of the interacting fragments are not trivial. The best fragmentation scheme to reflect the bonding situation in the molecule is understood by using the size of the orbital interaction (ΔE_{orb}) as a probe.[85–89] The fragments which give the lowest ΔE_{orb} value best reflect the actual bonding situation in the molecule since it requires the least change in the electronic charge of the fragments to obtain the electronic structure of the final molecule. Table S2† provides the numerical results of EDA considering Ga and Be_6Au_6 in different charges and electronic states as interacting fragments. An inspection of the relative size of the ΔE_{orb} value reveals that the most reasonable fragmentation scheme is Ga in the doublet state with the $4s^2 4p_\perp^1$ electronic configuration forming an electron-sharing π bond with the doublet $Be_6Au_6^+$ moiety. The detailed EDA–NOCV results of this most favorable scheme are tabulated in Table 1. The results show that one third of attractive interaction comes from the electrostatic interaction (ΔE_{elstat}), whereas two thirds of attraction originates from the covalent interaction. In fact, the repulsive interaction coming from the exchange term (Pauli repulsion, ΔE_{Pauli}) completely cancels the coulombic attraction.

The decomposition of ΔE_{orb} value into pairwise orbital interaction, $\Delta E_{orb(1)-(4)}$ in the EDA–NOCV method gives the most valuable information about bonding. The corresponding deformation densities are given in Fig. 4 which helps to assign the nature of bonds and involved orbitals. The results show that
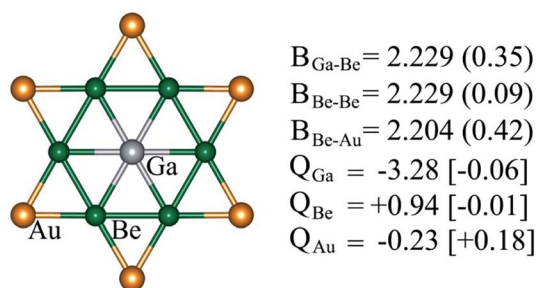

$B_{Ga-Be} = 2.229\ (0.35)$
$B_{Be-Be} = 2.229\ (0.09)$
$B_{Be-Au} = 2.204\ (0.42)$
$Q_{Ga} = -3.28\ [-0.06]$
$Q_{Be} = +0.94\ [-0.01]$
$Q_{Au} = -0.23\ [+0.18]$

Fig. 3 Bond properties (*B*, bond distances (Å), WBIs (in parentheses)), NPA and Hirshfeld (in square brackets) charges (*Q*, in |e|) of $GaBe_6Au_6^+$ computed at the PBE0/def2-TZVP level.

Table 1 The EDA–NOCV results of the $GaBe_6Au_6^+$ cluster considering Ga (D, $4s^24p_\perp^1$) and $Be_6Au_6^+$ (D) as interacting fragments at the PBE0/TZ2P-ZORA//PBE0/def2-ZVP level. Energy values are in kcal mol^{-1}

Energy	Interaction	Ga (D, $4s^24p_\perp^1$) + $Be_6Au_6^+$ (D)
ΔE_{int}	—	−261.6
ΔE_{Pauli}	—	137.1
$\Delta E_{elstat}{}^a$	—	−137.5 (34.5%)
$\Delta E_{orb}{}^a$	—	−261.1 (65.5%)
$\Delta E_{orb(1)}{}^b$	$Ga(p_\perp)$–$[Be_6Au_6^+]$ electron-sharing π-bond	−50.7 (19.4%)
$\Delta E_{orb(2)}{}^b$	$Ga(s) \rightarrow [Be_6Au_6^+]$ σ-backdonation	−78.5 (30.1%)
$\Delta E_{orb(3)}{}^b$	$Ga(p_\parallel) \leftarrow [Be_6Au_6^+]$ σ-donation	−61.0 (23.4%)
$\Delta E_{orb(4)}{}^b$	$Ga(p_\parallel) \leftarrow [Be_6Au_6^+]$ σ-donation	−60.8 (23.3%)
$\Delta E_{orb(rest)}{}^b$	—	−10.1 (3.9%)

[a] The percentage contribution with respect to total attraction is given in parentheses. [b] The percentage contribution in parentheses is given with respect to total orbital interaction.

the $Ga(p_\perp)$–$[Be_6Au_6^+]$ electron-sharing π-bond is responsible for 19.4% of total covalent interaction. This interaction involves the largest amount of electron as revealed by the charge eigenvalue, $|\nu|$ given in Fig. 4. Note that there is no correlation between electron involvement and stabilization energy as it will depend on the nature and orientation of the orbitals. The strongest orbital contribution (30.1%) comes from the $Ga(s) \rightarrow [Be_6Au_6^+]$ σ-backdonation. There are also two sets of $Ga(p_\parallel) \leftarrow [Be_6Au_6^+]$ σ-donations which together account for 46.7% of total orbital interaction. Therefore, in the $GaBe_6Au_6^+$ cluster the Ga center is involved in one electron-sharing bond and three dative bonds, and this bonding arrangement makes the actual oxidation state of Ga center as +1.

Now, why does only Ga enable the formation of phGa? To get an answer to this question we performed EDA–NOCV analysis for the whole set of $EBe_6Au_6^+$ cluster considering the phE isomer (see Table S3†). It is remarkable that the intrinsic interaction between E and $Be_6Au_6^+$ fragments is maximum for E = Ga, and the size of the ΔE_{orb} value also follows the same order. In Table S2,† we have also provided the steric interaction,[90] ΔE_{Steric} which is the sum of ΔE_{Pauli} and ΔE_{elstat}. ΔE_{Steric} values indicate that the coulombic attraction completely cancels the Pauli repulsion for E = Al and Ga but for E = In and Tl, because of their larger size, ΔE_{Steric} values are positive. Therefore, for the latter two cases, both steric interaction and smaller covalent interaction disfavor the phE isomer, while in
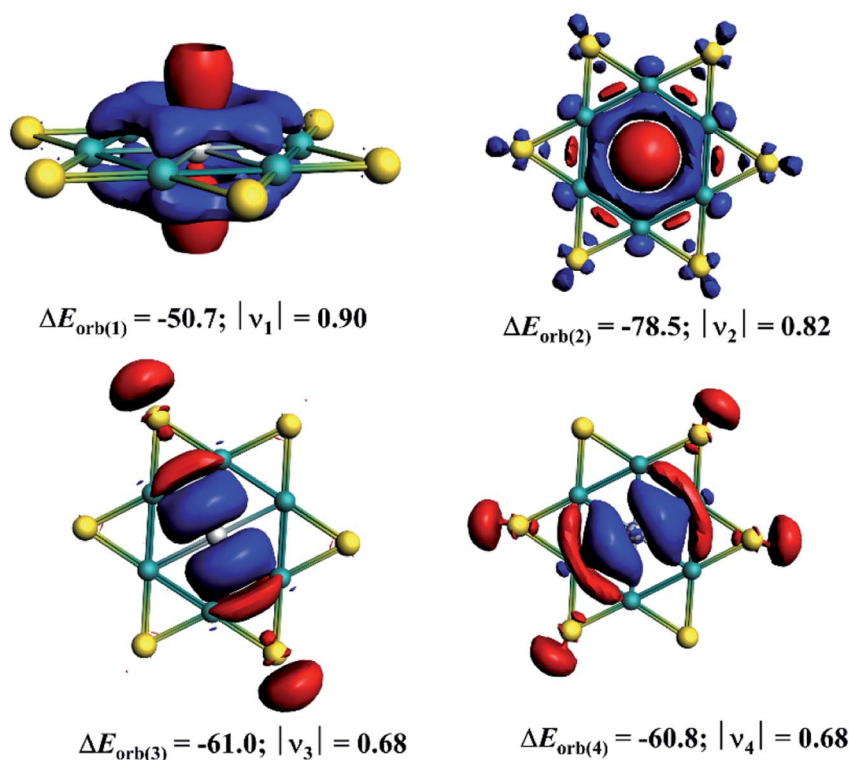

Fig. 4 The plot of the deformation densities $\Delta\rho_{(1)-(4)}$ corresponding to $\Delta E_{orb(1)-(4)}$ obtained from the EDA–NOCV calculations. The corresponding orbital value is given in kcal mol^{-1}. $|\nu|$ represents the charge eigenvalues. The electron moves from the red to blue region.

the case of E = Al, the smaller ΔE_{orb} value is the reason for this. This indicates that the size of the spatial distribution of p orbitals of E is also crucial for the strength of the bonding, and 4p orbitals seem to be in the right size to form bonds with the Be_6 ring. Also, the larger electronegativity of Ga compared to Al might be another reason for stronger $E(p_{\parallel}) \leftarrow [Be_6Au_6^+]$ σ-donation in the former than in the latter.

The remaining question: why is the C_{6v} isomer more stable than the D_{6h} one for the $InBe_6Au_6^+$ cluster while it is *vice versa* for the $TlBe_6Au_6^+$ cluster. To get the factors behind this, we performed EDA taking both the isomers (see Table S4†).[91] For the $InBe_6Au_6^+$ cluster, although the C_{6v} isomer possesses larger steric repulsion than the D_{6h} isomer, the larger ΔE_{orb} value of the former overcompensates that making it more stable than the latter one. In contrast, in the case of the $TlBe_6Au_6^+$ cluster, smaller steric repulsion in the D_{6h} isomer is responsible for making it slightly more stable than the C_{6v} isomer, although the latter has larger covalent interaction.

Electron delocalization

The adaptive natural density partitioning (AdNDP)[92] analysis was carried out for understanding the chemical bonding and electronic structure of global phGa. All the orbitals except for the d orbitals of Au are given in Fig. 5, and they basically can be divided into three categories. Six 3c–2e (three center-two electrons) σ bonds of the Be–Au–Be ring with occupation numbers (ONs) of 1.95|e| are responsible for the planarity and stability of the peripheral ring. The remaining orbitals are all associated with the central phGa atom, including three 7c–2e σ bonds with ONs of 1.97–1.98|e| and one 7c–2e π bond with ONs of 1.78|e|. Therefore, the valence shell of the central phGa atom has eight electrons, fulfilling the octet rule (3σ + 1π bonds). Meanwhile, phGa involves six delocalized σ electrons and two

delocalized π electrons, both satisfying the Hückel's $(4n + 2)$ rule for 6σ + 2π double aromaticity,[93] especially the latter (delocalization of the perpendicular p_z orbital of the central atom) can be viewed as the key factor of planarity.

The electron density distribution picture is further analyzed in the following tests. The diagram of electron localization function (ELF)[94] is shown in Fig. 6a, where the electron density is strongly localized in the $GaBe_6$ core, consistent with three σ and one π orbitals in this region. The contour plot of Laplacian distribution of the charge density $\nabla^2\rho(\mathbf{r})$ of $GaBe_6Au_6^+$ along with the bond critical points and ring critical points is shown in Fig. 6b. Note that the Ga–Be and peripheral Be–Au bonds possess clear bond critical points (blue dots), and the region with negative values of $\nabla^2\rho(\mathbf{r})$ located at the $GaBe_6$ core vividly confirm the covalent bonding picture.

To quantitatively evaluate the aromatic character in the phGa $GaBe_6Au_6^+$, the out-of-plane tensor components of the nucleus-independent chemical shift $(NICS_{zz})$[95] were considered as displayed in Fig. 6. In the picture, the diatropic NICS tensors on and above the plane of phGa in 1 Å interval up to 3 Å are given as red spheres, whereas the paratropic tensors are depicted by the green spheres. Inside the hexagon, at three points, *viz.*, at the center of the Be–Be–Ga triangle, at the middle pint of the Be–Ga bond, and at the phGa center, the shielding tensors are computed. As reflected from Fig. 6c, the full hexagon is located in a moderate diatropic region, whereas the outside region of the hexagonal ring has a paratropic response. Focusing on the Be–Be–Ga triangle, $NICS_{zz}(0)$ is −9.5 ppm and $NICS_{zz}(1)$ is −11.9 ppm. The $NICS_{zz}$ values decrease along with the increasing distances from the molecular plane. But even at 3 Å above the triangular plane, it still has considerable diatropic response. Note that the phGa center is itself located at a very strong diatropic region as indicated by the very negative $NICS_{zz}$ values. An inspection of results of canonical molecular orbital (CMO)-$NICS_{zz}$ originating from the one π and three σ delocalized orbitals indicate that the diatropic contribution from the delocalized π orbital is rather small with an $NICS_{\pi zz}(1)$ value of −9.1 ppm above the phGa center and −4.6 ppm above the Be–Be–Ga triangle (see Fig. 6d). Note that similar analysis was used to elucidate the aromaticity in the CAl_5^+ cluster with ppC by Schleyer and Zeng and co-workers.[19] The results of CMO-$NICS_{zz}$ in the CAl_5^+ cluster are very similar to the present one where the diatropic contribution developed from the delocalized π orbital is rather small ($NICS_{\pi zz}(1)$: −11.5 ppm above ppC and −4.3 ppm above the center of the C–Al–Al triangle). In fact, the comparison of the $NICS_{\pi zz}$ profile between these two systems shows that the magnetic response at 2 Å and 3 Å above the present phGa center is more diatropic in nature than those above the ppC center. This is presumably because in the former cluster the $4p_z$ orbital is involved while in the latter case the smaller $2p_z$ orbital is engaged. Note that both phGa and ppC clusters are significantly less π aromatic than the prototype aromatic system, benzene (see Fig. S8†). The tensor contribution from the delocalized σ-orbitals is more diatropic in nature (see Fig. 6e). This highlights the greater importance of σ-delocalization than the π-delocalization for the stabilization of the planar form. The shape of delocalized σ and π CMOs is also displayed in Fig. 6f.
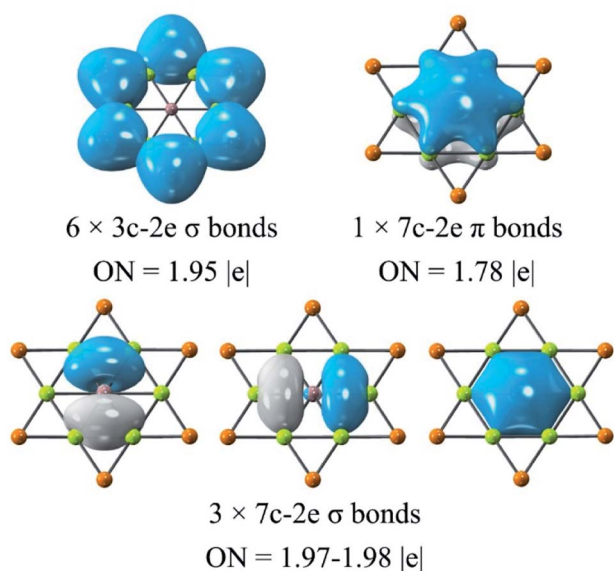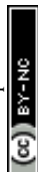

Fig. 5 AdNDP analysis of phGa $GaBe_6Au_6^+$ computed at the PBE0/def2-TZVP level. Occupation number (ON) values are shown in |e|.
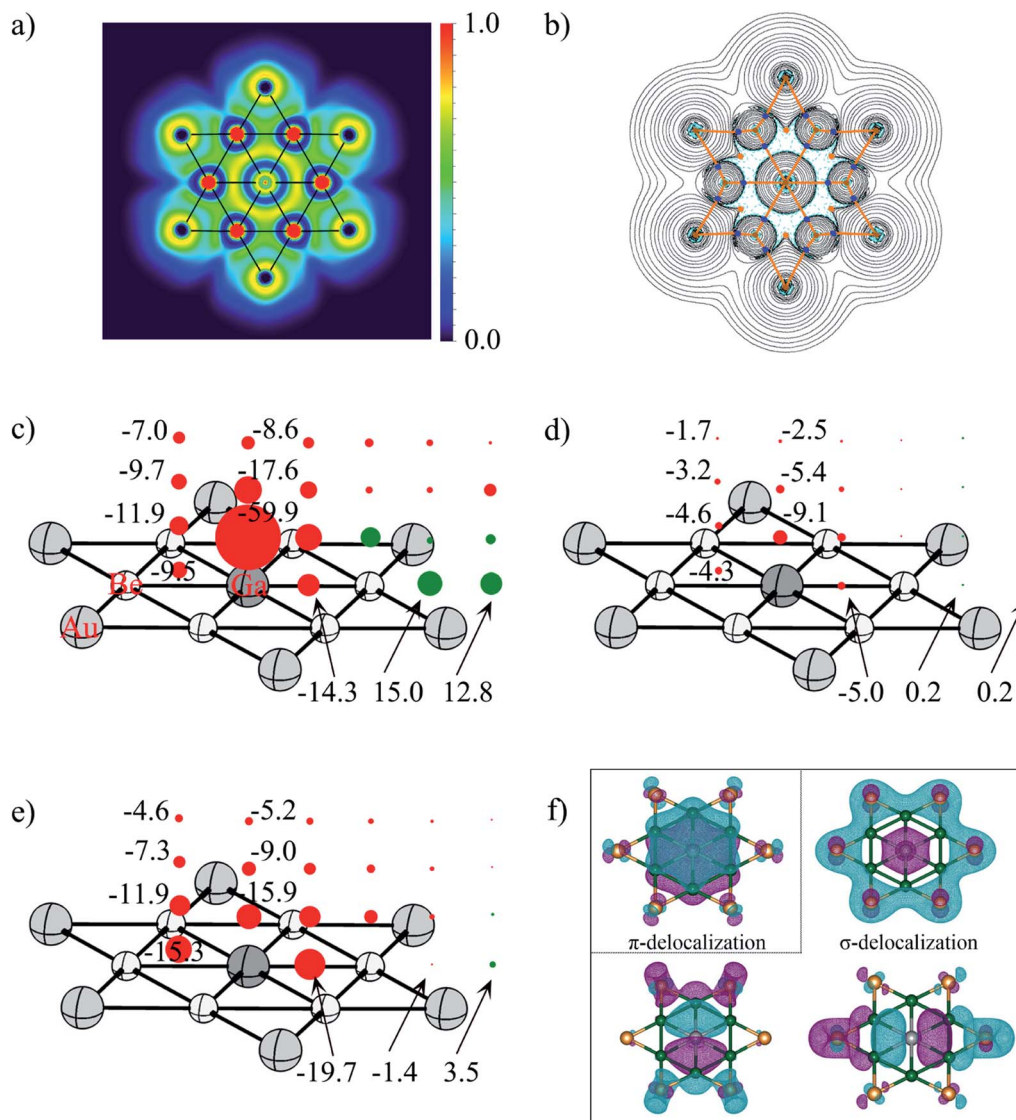
Fig. 6 (a) Electron localization function (ELF) and (b) the contour plot of the Laplacian distribution of electron density, $\nabla^2\rho(r)$ including bond critical points and bond paths of phGa, where cyan dashed lines indicate areas of charge concentration ($\nabla^2\rho(r) < 0$) and solid black lines show areas of charge depletion ($\nabla^2\rho(r) > 0$). The solid orange lines connecting the atomic nuclei are the bond paths. Blue dots are bond critical points (BCPs), and orange dots are ring critical points (RCPs); (c) NICS$_{zz}$, (d) NICS$_{\pi zz}$, (e) NICS$_{\sigma zz}$ (σ-delocalization) and (f) the shape of π-delocalized CMO and three σ-delocalized CMOs of the D_{6h} GaBe$_6$Au$_6^+$ at the PBE0/def2-TZVP level (the values in the left column refer to the center of the Be–Ge–Be triangle). Diatropic and paratropic tensors are shown in red and green, respectively. NICS values are in ppm.

Therefore, the magnetic response of the cluster corroborates with the number of delocalized σ and π electrons. It is interesting to note that the much higher energy phTl isomer is also doubly aromatic (see Fig. S9†) which implies that the aromaticity is not solely a predetermining factor to stabilize the planar form, rather the delicate balance between the size of the atom and its ability to form strong bonds with the outer ring are important.

Conclusions

We herein report the first phGa center in the most stable isomer of the GaBe$_6$Au$_6^+$ cluster by systematically exploring the potential energy surface of the full set of the EBe$_6$Au$_6^+$ (E = Al, Ga, In,

Tl) cluster. The global minimum of the GaBe$_6$Au$_6^+$ cluster has a star-like D_{6h} geometry with $^1A_{1g}$ electronic state, possessing a centered Ga atom encompassed by a Be$_6$ hexagon and each Be–Be edge is further capped by an Au atom. The present results also show that among group 13 elements, Ga can form the strongest bonds with the hexagonal ring in the D_{6h} symmetric isomer, and, thus it facilitates the drastic reorientation of the Be$_6$Au$_6$ cluster which has a three-dimensional geometry as the lowest energy isomer. The planarization of the GaBe$_6$Au$_6^+$ cluster is well supported by the three delocalized σ bonds and one delocalized π bond which individually satisfy Hückel's rule of aromaticity. Furthermore, the CMO-NICS$_{zz}$ values corroborate with the double aromaticity assignment. The large barrier against isomerization is also reflected from the BO-MD
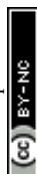
simulations performed at 300 and 400 K. The energy decomposition analysis in combination with the natural orbitals for chemical valence theory reveals that the bonding in the $GaBe_6Au_6^+$ cluster is best expressed as the doublet Ga atom with $4s^2 4p_\perp^1$ electronic configuration forming an electron-sharing π bond with the doublet $Be_6Au_6^+$ moiety followed by $Ga(s) \rightarrow [Be_6Au_6^+]$ σ-backdonation and two sets of $Ga(p_\parallel) \leftarrow [Be_6Au_6^+]$ σ-donations. We hope that the current findings will provide useful information for obtaining the rule-breaking planar hypercoordinate clusters.

Data availability

All our computational data is already included in the ESI† and in the videos for the BO-MD runs.

Author contributions

M.-h. W. and C. C. performed the computations. S. P. and Z.-h. C. analyzed the results and wrote the draft.

Conflicts of interest

The authors declare no conflict of interest.

Acknowledgements

References

1 R. Hoffmann, R. W. Alder and C. F. Wilcox, *J. Am. Chem. Soc.*, 1970, **92**, 4492–4493.

2 V. Vassilev-Galindo, S. Pan, K. J. Donald and G. Merino, *Nat. Rev. Chem.*, 2018, **2**, 1–10.

3 L. M. Yang, E. Ganz, Z. F. Chen, Z. X. Wang and P. V. Schleyer, *Angew. Chem., Int. Ed.*, 2015, **54**, 9468–9501.

4 G. Merino, M. A. Mendez-Rojas, A. Vela and T. Heine, *J. Comput. Chem.*, 2007, **28**, 362–372.

5 R. Keese, *Chem. Rev.*, 2006, **106**, 4787–4808.

6 W. Siebert and A. Gunale, *Chem. Soc. Rev.*, 1999, **28**, 367–371.

7 G. Erker, *Chem. Soc. Rev.*, 1999, **28**, 307–314.

8 J. J. Sui, J. Xu and Y. H. Ding, *Dalton T*, 2016, **45**, 56–60.

9 A. I. Boldyrev, X. Li and L. S. Wang, *Angew. Chem., Int. Ed.*, 2000, **39**, 3307–3310.

10 E.-U. Würthwein and P. V. R. Schleyer, *Angew. Chem., Int. Ed.*, 1979, **18**, 553–554.

11 H. Y. Wang and F. L. Liu, *Acs Omega*, 2020, **5**, 24513–24519.

12 Z. C. Liu, J. Y. Lei, M. Frasconi, X. H. Li, D. Cao, Z. X. Zhu, S. T. Schneebeli, G. C. Schatz and J. F. Stoddart, *Angew. Chem., Int. Ed.*, 2014, **53**, 9193–9197.

13 G. Castillo-Toraya, M. Orozco-Ic, E. Dzib, X. Zarate, F. Ortiz-Chi, Z. H. Cui, J. Barroso and G. Merino, *Chem. Sci.*, 2021, **12**, 6699–6704.

14 W. Feng, C. Y. Zhu, X. M. Liu, M. Zhang, Y. Geng, L. Zhao and Z. M. Su, *New J. Chem.*, 2020, **44**, 767–772.

15 F. Ebner, H. Wadepohl and L. Greb, *J. Am. Chem. Soc.*, 2019, **141**, 18009–18012.

16 P. Ghana, J. Rump, G. Schnakenburg, M. I. Arz and A. C. Filippou, *J. Am. Chem. Soc.*, 2021, **143**, 420–432.

17 F. Ebner and L. Greb, *Chem*, 2021, **7**, 2151–2159.

18 F. Ebner and L. Greb, *J. Am. Chem. Soc.*, 2018, **140**, 17409–17412.

19 Y. Pei, W. An, K. Ito, P. V. Schleyer and X. C. Zeng, *J. Am. Chem. Soc.*, 2008, **130**, 10394–10400.

20 Z. X. Wang and P. V. Schleyer, *Science*, 2001, **292**, 2465–2469.

21 M. H. Wang, X. Dong, Z. H. Cui, M. Orozco-Ic, Y. H. Ding, J. Barroso and G. Merino, *Chem. Commun.*, 2020, **56**, 13772–13775.

22 A. J. Kalita, S. S. Rohman, C. Kashyap, S. S. Ullah, I. Baruah and A. K. Guha, *Inorg. Chem.*, 2020, **59**, 17880–17883.

23 L. Leyva-Parra, L. Diego, O. Yañez, D. Inostroza, J. Barroso, A. Vásquez-Espinal, G. Merino and W. Tiznado, *Angew. Chem., Int. Ed.*, 2020, **133**, 8782–8786.

24 Y. B. Wu, Y. Duan, G. Lu, H. G. Lu, P. Yang, P. V. Schleyer, G. Merino, R. Islas and Z. X. Wang, *Phys. Chem. Chem. Phys.*, 2012, **14**, 14760–14763.

25 K. Exner and P. V. Schleyer, *Science*, 2000, **290**, 1937–1940.

26 A. J. Kalita, S. S. Rohman, C. Kashyap, S. S. Ullah and A. K. Guha, *Chem. Commun.*, 2020, **56**, 12597–12599.

27 X. F. Zhao, J. J. Li, H. R. Li, C. X. Yuan, X. X. Tian, S. D. Li, Y. B. Wu, J. C. Guo and Z. X. Wang, *Phys. Chem. Chem. Phys.*, 2018, **20**, 7217–7222.

28 A. I. Boldyrev and J. Simons, *J. Am. Chem. Soc.*, 1998, **120**, 7967–7972.

29 P. v. R. Schleyer and A. Boldyrev, *J. Chem. Soc., Chem. Commun.*, 1991, **21**, 1536–1538.

30 H. F. Zheng, J. Xu and Y. H. Ding, *Phys. Chem. Chem. Phys.*, 2020, **22**, 3975–3982.

31 J. C. Guo, L. Y. Feng and H. J. Zhai, *New J. Chem.*, 2020, **44**, 18293–18302.

32 E. Ravell, S. Jalife, J. Barroso, M. Orozco-Ic, G. Hernandez-Juarez, F. Ortiz-Chi, S. Pan, J. L. Cabellos and G. Merino, *Chem.-Asian. J.*, 2018, **13**, 1467–1473.

33 J. C. Guo, L. Y. Feng and H. J. Zhai, *Phys. Chem. Chem. Phys.*, 2018, **20**, 6299–6306.

34 O. Yanez, A. Vasquez-Espinal, R. Pino-Rios, F. Ferraro, S. Pan, E. Osorio, G. Merino and W. Tiznado, *Chem. Commun.*, 2017, **53**, 12112–12115.

35 M. Contreras, S. Pan, M. Orozco-Ic, J. L. Cabellos and G. Merino, *Chem.–Eur. J.*, 2017, **23**, 11430–11436.

36 Y. B. Wu, Z. X. Li, X. H. Pu and Z. X. Wang, *Comput. Theor. Chem.*, 2012, **992**, 78–83.

37 A. C. Castro, M. Audiffred, J. M. Mercero, J. M. Ugalde, M. A. Mendez-Rojas and G. Merino, *Chem. Phys. Lett.*, 2012, **519**, 29–33.

38 Y. B. Wu, Z. X. Li, X. H. Pu and Z. X. Wang, *J. Phys. Chem. C*, 2011, **115**, 13187–13192.

39 Y. B. Wu, J. L. Jiang, H. G. Lu, Z. X. Wang, N. Perez-Peralta, R. Islas, M. Contreras, G. Merino, J. I. C. Wu and P. V. Schleyer, *Chem.–Eur. J.*, 2011, **17**, 714–719.

40 Z. H. Cui, M. Contreras, Y. H. Ding and G. Merino, *J. Am. Chem. Soc.*, 2011, **133**, 13228–13231.

41 P. D. Pancharatna, M. A. Mendez-Rojas, G. Merino, A. Vela and R. Hoffmann, *J. Am. Chem. Soc.*, 2004, **126**, 15309–15315.

42 G. Merino, M. A. Mendez-Rojas, H. I. Beltraan, C. Corminboeuf, T. Heine and A. Vela, *J. Am. Chem. Soc.*, 2004, **126**, 16160–16169.

43 S.-D. Li, G.-M. Ren, C.-Q. Miao and H.-J. Zhai, *Angew. Chem., Int. Ed.*, 2004, **43**, 1371–1373.

44 Y. Sahin, C. Prasang, M. Hofmann, G. Subramanian, G. Geiseler, W. Massa and A. Berndt, *Angew. Chem., Int. Ed.*, 2003, **42**, 671–674.

45 G. Merino, M. A. Mendez-Rojas and A. Vela, *J. Am. Chem. Soc.*, 2003, **125**, 6026–6027.

46 J. Xu, X. Zhang, S. Yu, Y. H. Ding and K. H. Bowen, *J. Phys. Chem. Lett.*, 2017, **8**, 2263–2267.

47 X. Li, H. J. Zhai and L. S. Wang, *Chem. Phys. Lett.*, 2002, **357**, 415–419.

48 X. Li, H. F. Zhang, L. S. Wang, G. D. Geske and A. I. Boldyrev, *Angew. Chem., Int. Ed.*, 2000, **39**, 3630–3633.

49 A. I. Boldyrev, X. Li and L. S. Wang, *Angew. Chem., Int. Ed.*, 2000, **39**, 3445–3448.

50 X. Li, L. S. Wang, A. I. Boldyrev and J. Simons, *J. Am. Chem. Soc.*, 1999, **121**, 6033–6038.

51 O. Yanez, R. Baez-Grez, J. Garza, S. Pan, J. Barroso, A. Vasquez-Espinal, G. Merino and W. Tiznado, *Chemphyschem*, 2020, **21**, 145–148.

52 M. H. Wang, X. Dong, Y. H. Ding and Z. H. Cui, *Chem. Commun.*, 2020, **56**, 7285–7288.

53 J. C. Guo, L. Y. Feng, J. Barroso, G. Merino and H. J. Zhai, *Chem. Commun.*, 2020, **56**, 8305–8308.

54 S. Pan, J. L. Cabellos, M. Orozco-Ic, P. K. Chattaraj, L. L. Zhao and G. Merino, *Phys. Chem. Chem. Phys.*, 2018, **20**, 12350–12355.

55 J. C. Guo, L. Y. Feng, X. Y. Zhang and H. J. Zhai, *J. Phys. Chem. A*, 2018, **122**, 1138–1145.

56 Z. H. Cui, V. Vassilev-Galindo, J. L. Cabellos, E. Osorio, M. Orozco, S. Pan, Y. H. Ding and G. Merino, *Chem. Commun.*, 2017, **53**, 138–141.

57 J. C. Guo, G. M. Ren, C. Q. Miao, W. J. Tian, Y. B. Wu and X. T. Wang, *J. Phys. Chem. A*, 2015, **119**, 13101–13106.

58 Y. B. Wu, Y. Duan, H. G. Lu and S. D. Li, *J. Phys. Chem. A*, 2012, **116**, 3290–3294.

59 J. O. C. Jimenez-Halla, Y. B. Wu, Z. X. Wang, R. Islas, T. Heine and G. Merino, *Chem. Commun.*, 2010, **46**, 8776–8778.

60 B. B. Averkiev, D. Y. Zubarev, L. M. Wang, W. Huang, L. S. Wang and A. I. Boldyrev, *J. Am. Chem. Soc.*, 2008, **130**, 9248–9250.

61 H. J. Zhai, A. N. Alexandrova, K. A. Birch, A. I. Boldyrev and L. S. Wang, *Angew. Chem., Int. Ed.*, 2003, **42**, 6004–6008.

62 C. J. Zhang, H. G. Xu, X. L. Xu and W. J. Zheng, *J. Phys. Chem. A*, 2021, **125**, 302–307.

63 B. J. Feng, B. T. Fu, S. Kasamatsu, S. Ito, P. Cheng, C. C. Liu, Y. Feng, S. L. Wu, S. K. Mahatha, P. Sheverdyaeva, P. Moras, M. Arita, O. Sugino, T. C. Chiang, K. Shimada, K. Miyamoto, T. Okuda, K. H. Wu, L. Chen, Y. G. Yao and I. Matsuda, *Nat. Commun.*, 2017, **8**, 1–6.

64 L. M. Yang, V. Bačić, I. A. Popov, A. I. Boldyrev, T. Heine, T. Frauenheim and E. Ganz, *J. Am. Chem. Soc.*, 2015, **137**, 2757–2762.

65 Y. Wang, Y. Li and Z. Chen, *Acc. Chem. Res.*, 2020, **53**, 887–895.

66 Y. C. Wang, J. Lv, L. Zhu and Y. M. Ma, *Comput. Phys. Commun.*, 2012, **183**, 2063–2070.

67 J. Lv, Y. C. Wang, L. Zhu and Y. M. Ma, *J. Chem. Phys.*, 2012, **137**, 084104.

68 C. Adamo and V. Barone, *J. Chem. Phys.*, 1999, **110**, 6158–6170.

69 F. Weigend and R. Ahlrichs, *Phys. Chem. Chem. Phys.*, 2005, **7**, 3297–3305.

70 J. A. Pople, M. Head-Gordon and K. Raghavachari, *J. Chem. Phys.*, 1987, **87**, 5968–5975.

71 M. J. Frisch, G. W. Trucks, H. B. Schlegel, G. E. Scuseria, M. A. Robb, J. R. Cheeseman, G. Scalmani, V. Barone, B. Mennucci, G. A. Petersson, H. Nakatsuji, M. Caricato, X. Li, H. P. Hratchian, A. F. Izmaylov, J. Bloino, G. Zheng, J. L. Sonnenberg, M. Hada, M. Ehara, K. Toyota, R. Fukuda, J. Hasegawa, M. Ishida, T. Nakajima, Y. Honda, O. Kitao, H. Nakai, T. Vreven, J. A. Montgomery, J. E. Peralta, F. Ogliaro, M. Bearpark, J. J. Heyd, E. Brothers, K. N. Kudin, V. N. Staroverov, R. Kobayashi, J. Normand, K. Raghavachari, A. Rendell, J. C. Burant, S. S. Iyengar, J. Tomasi, M. Cossi, N. Rega, N. J. Millam, M. Klene, J. E. Knox, J. B. Cross, V. Bakken, C. Adamo, J. Jaramillo, R. Gomperts, R. E. Stratmann, O. Yazyev, A. J. Austin, R. Cammi, C. Pomelli, J. W. Ochterski, R. L. Martin, K. Morokuma, V. G. Zakrzewski, G. A. Voth, P. Salvador, J. J. Dannenberg, S. Dapprich, A. D. Daniels, O. Farkas, J. B. Foresman, J. V. Ortiz, J. Cioslowski and D. J. Fox, *Gaussian 09, Revision D.01*, Gaussian, Inc, Wallingford CT, 2009.

72 A. E. Reed, R. B. Weinstock and F. Weinhold, *J. Chem. Phys.*, 1985, **83**, 735–746.

73 K. B. Wiberg, *Tetrahedron*, 1968, **24**, 1083–1096.

74 E. D. Glendening, C. R. Landis and F. Weinhold, *J. Comput. Chem.*, 2019, **40**, 2234–2241.

75 F. Corts-Guzman and R. F. W. Bader, *Coord. Chem. Rev.*, 2005, **249**, 633–662.

76 R. F. W. Bader, *Chem. Rev.*, 1991, **91**, 893–928.

77 T. Lu and F. Chen, *J. Comput. Chem.*, 2012, **33**, 580–592.

78 J. M. Millam, V. Bakken, W. Chen, W. L. Hase and H. B. Schlegel, *J. Chem. Phys.*, 1999, **111**, 3800–3805.

79 T. Ziegler and A. Rauk, *Theor. Chim. Acta*, 1977, **46**, 1–10.

80 M. Mitoraj and A. Michalak, *Organometallics*, 2007, **26**, 6576–6580.

81 G. te Velde, F. M. Bickelhaupt, E. J. Baerends, C. F. Guerra, S. J. A. Van Gisbergen, J. G. Snijders and T. Ziegler, *J. Comput. Chem.*, 2001, **22**, 931–967.

82 ADF2018, *SCM, Theoretical Chemistry*, Vrije Universiteit, Amsterdam, The Netherlands, http://www.scm.com.

83 L. L. Zhao, S. Pan, N. Holzmann, P. Schwerdtfeger and G. Frenking, *Chem. Rev.*, 2019, **119**, 8781–8845.

84 P. Pyykkö, *J. Phys. Chem. A*, 2015, **119**, 2326–2337.

85 W. L. Yang, K. E. Krantz, L. A. Freeman, D. A. Dickie, A. Molino, G. Frenking, S. D. Pan, D. J. D. Wilson and R. J. Gilliard, *Angew. Chem., Int. Ed.*, 2020, **59**, 3850–3854.

86 R. Saha, S. Pan, P. K. Chattaraj and G. Merino, *Dalton Trans.*, 2020, **49**, 1056–1064.

87 S. M. N. V. T. Gorantla, S. Pan, K. C. Mondal and G. Frenking, *Chem.–Eur. J.*, 2020, **26**, 14211–14220.

88 L. Pecher, S. Pan and G. Frenking, *Theor. Chem. Acc.*, 2019, **138**, 47.

89 C. X. Chi, S. Pan, L. Y. Meng, M. B. Luo, L. L. Zhao, M. F. Zhou and G. Frenking, *Angew. Chem., Int. Ed.*, 2019, **58**, 1732–1738.

90 For more information the readers are referred to F. M. Bickelhaupt and E. J. Baerends, Kohn-Sham Density Functional Theory: Predicting and Understanding Chemistry, in: *Rev. Comput. Chem*, ed. K. B. Lipkowitz and D. B. Boyd, Wiley-VCH, New York, 2000, vol. 15, pp. 1–86.

91 Note that for $TlBe_6Au_6^+$ cluster, the imposed C_{6v} isomer is automatically converged to planar D_{6h} isomer during optimization. Although the job with transition state optimization is not fully converged, it was nearly converged. Only one parameter, maximum force (0.000544) does not fall under the threshold value (0.000450). We took that structure and performed frequency calculation and found that all are real. Since this structure is very close to stationary point, it does not alter the total electronic energy.

92 D. Y. Zubarev and A. I. Boldyrev, *Phys. Chem. Chem. Phys.*, 2008, **10**, 5207–5217.

93 J. Chandrasekhar, E. D. Jemmis and P. v. R. Schleyer, *Tetrahedron Lett.*, 1979, **20**, 3707–3710.

94 A. Savin, R. Nesper, S. Wengert and T. F. Fassler, *Angew. Chem., Int. Ed.*, 1997, **109**, 1892–1918.

95 Z. F. Chen, C. S. Wannere, C. Corminboeuf, R. Puchta and P. V. Schleyer, *Chem. Rev.*, 2005, **105**, 3842–3888.